Nonideal effects on ionization potential depression and ionization balance in dense Al and Au plasmas

Yihua Huang [,1] Zhenhao Liang [,1] Jiaolong Zeng [,1,*] and Jianmin Yuan [2,3,†]

[1]*College of Science, Zhejiang University of Technology, Hangzhou Zhejiang 310023, People's Republic of China*
[2]*Institute of Atomic and Molecular Physics, Jilin University, Changchun Jilin 130012, People's Republic of China*
[3]*Graduate School of China Academy of Engineering Physics, Beijing 100193, People's Republic of China*

For low-density plasmas, the ionization balance can be properly described by the normal Saha equation in the chemical picture. For dense plasmas, however, nonideal effects due to the interactions between the electrons and ions and among the electrons themselves affect the ionization potential depression and the ionization balance. With the increasing of plasma density, the pressure ionization starts to play a more obvious role and competes with the thermal ionization. Based on a local-density temperature-dependent ion-sphere model, we develop a unified and self-consistent theoretical formalism to simultaneously investigate the ionization potential depression, the ionization balance, and the charge states distributions of the dense plasmas. In this work, we choose Al and Au plasmas as examples as Al is a prototype light element and Au is an important heavy element in many research fields such as in the inertial confinement fusion. The nonideal effect of the free electrons in the plasmas is considered by the single-electron effective potential contributed by both the bound electrons of different charge states and the free electrons in the plasmas. For the Al plasmas, we can reconcile the results of two experiments on measuring the ionization potential depression, in which one experiment can be better explained by the Stewart-Pyatt model while the other fits better with the Ecker-Kröll model. For dense Au plasmas, the results show that the double peak structure of the charge state distribution appears to be a common phenomenon. In particular, the calculated ionization balance shows that the two- and three-peak structures can appear simultaneously for denser Au plasmas above $\sim$30 g/cm^3.

I. INTRODUCTION

Dense plasmas exist widely in nature and in scientific laboratories. In astrophysical objects such as the stellar interiors and the envelopes and cores of brown dwarfs [1,2], the plasma mass density ranges from 0.1 g/cm^3 to higher than 1000 g/cm^3. In the inertial confinement fusion (ICF) investigations [3,4], the mass density of the plasma can vary from a lower one to a higher one of a few hundred g/cm^3 in different stages. With the development of experimental technologies, it is now possible to study the properties of dense plasmas quantitatively in laboratories. The newly developed x-ray free electron lasers (XFELs) make it practical to measure the ionization potential depression (IPD) of solid density plasmas [5–7]. One newly commissioned study on the Orion laser system was carried out on measuring the IPDs of dense plasmas in a density range of 1–10 g/cm^3 by combining a short-pulse laser heating and a laser-driven shock compression [8]. Detailed measurements of the IPDs of carbon ions are achieved with spectrally resolved x-ray scattering for dense CH plasmas with a density of up to $\sim$9 g/cm^3 during the transient state of the three-shock coalescence [9]. The average degree of ionization of dense carbon plasmas with a density up to $\sim$7 g/cm^3 created by spherically convergent shocks at the National Ignition Facility was measured using the spectrally resolved x-ray scattering technique [10]. The average degree of ionization of dense Be plasmas at mass densities up to 55 g/cm^3 reached 30 times of compression was measured using the x-ray scattering technique [11]. The onset of the K-shell delocalization is the precursor of the pressure ionization and has been observed experimentally. Although these great achievements have been obtained, detailed measurements on the ionization balance to obtain the population fractions quantitatively of different charge states in dense plasmas is still challenging and awaits further investigations.

The great achievements in experimental investigations on the IPDs and the ionization balance deepen our understanding towards the dense plasmas. However, the physics behind these experimental findings has not been well understood up to now. For the IPD, the predictions by the traditional analytical models [12,13] cannot reconcile the experimental findings [5,6,8]. The experiment [5] performed at the Linac Coherent Light Source (LCLS) [14] shows that the Ecker-Kröll (EK) model [13] is in closer agreement with the experiment than the Stewart-Pyatt (SP) model [12]. However, one later experiment also at LCLS shows that the EK model cannot explain the IPDs of Mg and Al compounds [6]. A laser-driven shock experiment [8] at the ORION laser system shows that the SP model [12] can better explain the experiment than the EK

model [13], although the SP model cannot fully interpret the measured emissivity in the experiment. These investigations indicate that the previous traditional analytical models on predicting the IPDs are difficult to capture the essential physics of the dense plasmas, which stimulate a variety of theoretical investigations on the IPDs of dense plasmas [15–32]. Though these theoretical efforts have resolved some of the controversial issues on the IPDs of dense plasmas, much fewer renewed efforts have been made on resolving the ionization balance. In comparison with the experiment [10], the traditional models including the Thomas-Fermi and the SP failed to reproduce the measured average degree of ionization. As mentioned by the authors of this experiment [10], there is no reliable and practical *ab initio* technique so far to obtain any predictions for the plasma regime probed in their experiment. The same thing can be found in the experiment in Ref. [11], where the SP and the OPAL [33] models cannot correctly describe the ionization balance for Be plasmas at mass densities ranging from 6 to 55 g/cm^3.

Accurate theoretical description of the IPD and the ionization balance of dense plasmas in local thermodynamic equilibrium (LTE) is of fundamental interest as the macroscopic properties of such systems depend crucially on the ionization balance. Although ongoing efforts have been carried out to study the matter, it is still difficult to accurately predict the ionization balance of dense plasmas [1,10,11]. One reason for this is the complex physics related to the quantum many-body effects still awaiting further exploration. In particular, the IPD and the ionization balance are closely interrelated with each other and hence a unified and self-consistent theoretical formalism is needed to treat them.

x-Ray spectroscopy of dense plasmas is essential to our fundamental understanding of how matter behaves at extreme conditions [34] and it provides a valuable diagnostic tool for plasma conditions [35,36]. Other useful information can also be obtained from x-ray spectroscopy such as inference of ignition-relevant fuel areal densities in ICF capsule implosion experiments [37] and constraint of the ionization-potential depression models [38]. Novel emission and absorption mechanisms of interspecies radiative transitions are predicted to emerge in superdense plasmas [39]. It is well known that all these important applications need reliable information on ionization balance.

In one of our previous works, we extended the ionization balance equation in the chemical picture [40–47] to a dense regime by introducing the effect of nonideal characteristics (NIC) on the partition functions of free electrons in the plasmas [48], with using iron plasma as an example. The research results show that the extended theoretical formalism successfully interpreted the measured opacity of dense C_9H_{10} plasma at a photon energy of 9 keV [1], validating the effectiveness of the proposed theory. Herein, we investigate the IPD and the ionization balance in dense Al and Au plasmas based on a unified and self-consistent theoretical formalism. In this formalism, the required physical quantities in the ionization balance, including the energy levels, the ionization potential, and the partition functions of the ions and free electrons, are obtained in a self-consistent way. The IPD, mean ionization, and level populations are calculated self-consistently at

a given plasma temperature and density by using the same plasma screening potential utilized in calculating the bound and free electronic states of different charge states.

II. THEORETICAL METHODS

For an ion embedded in a dense plasma, the wave functions of its electron orbitals are determined by solving the relativistic quantum mechanical equations [49,50] (atomic units are used unless specified otherwise),

$$[H_0 + V_{scr}(r)]\psi(\boldsymbol{r}) = E_i\psi(\boldsymbol{r}), \tag{1}$$

where H_0 is the Hamiltonian of the corresponding isolated ion for the potential due to its nuclear charge and all the bound electrons,

$$H_0 = \sum_{i=1}^{N} H_D(i) + \sum_{i<j}^{N} \frac{1}{r_{ij}}, \tag{2}$$

where N denotes the number of bound electrons and $H_D(i)$ is the one-body contribution of the ith electron to the atomic Hamiltonian including the kinetic energy and interaction potential with the nucleus. An additional screening potential $V_{scr}(r)$ is added into the Hamiltonian of the isolated ion to describe the plasma environment effect. In a dense plasma, such a screening potential is in general not as trivial as a perturbation and hence should be directly included into the quantum mechanical equations from the beginning of calculating the wave functions. When the plasma screening potential $V_{scr}(r)$ was dropped, Eq. [1] corresponds to the isolated ion case.

The basis states of the atomic wave functions are constructed from the products of N one-electron Dirac spinors,

$$\varphi_{n\kappa m} = \frac{1}{r}\begin{bmatrix} P_{n\kappa}(r)\chi_{\kappa m}(\theta, \psi, \sigma) \\ iQ_{n\kappa}(r)\chi_{-\kappa m}(\theta, \psi, \sigma) \end{bmatrix}, \tag{3}$$

where $P_{n\kappa}(r)$ and $Q_{n\kappa}(r)$ are the large and small components of the radial wave functions; $\chi_{\kappa m}(\theta, \psi, \sigma)$ is a two-component spherical spinor; and n, κ, and m denote the principal, the relativistic angular, and the magnetic quantum numbers of the electron orbital, respectively. In the central-potential approximation, the large and small components of the radial wave function satisfy the coupled Dirac equations,

$$\left(\frac{d}{dr} + \frac{\kappa}{r}\right)P_{n\kappa} = \alpha\left[\varepsilon_{n\kappa} - V(r) + \frac{2}{\alpha^2}\right]Q_{n\kappa}$$

$$\left(\frac{d}{dr} - \frac{\kappa}{r}\right)Q_{n\kappa} = \alpha[-\varepsilon_{n\kappa} + V(r)]P_{n\kappa}, \tag{4}$$

where α denotes the fine-structure constant and $\varepsilon_{n\kappa}$ is the energy eigenvalue of the electron orbital. The local central potential $V(r)$ includes both the single-electron effective potential of the isolated ion and the screening potential from the plasma environment.

In a dense plasma in the LTE, the plasma screening potential $V_{scr}(r)$ is assumed to be predominantly contributed by the density function of the free electrons $\rho(r)$ in the plasma

[16,30,31,51],

$$V_{\text{scr}}(r) = 4\pi \left[\frac{1}{r} \int_0^r r_1 + \int_r^{R_0} r_1 \rho(r_1) \right] dr_1 - \frac{3}{2} \left[\frac{3}{\pi} \rho(r) \right]^{1/3},$$

(5)

where Z is the nuclear charge and the last term in the above equation representing the Slater exchange potential. The radius of the ion sphere is determined by the ion number density n_i,

$$R_0 = \left(\frac{3}{4\pi n_i} \right)^{\frac{1}{3}}.$$

(6)

The density function $\rho(r)$ of the free electrons is determined by the ionization balance in the plasma and obeys the Fermi-Dirac distribution,

$$\rho(r) = \frac{1}{\pi^2} \int_{k_0(r)}^{\infty} \frac{k^2 dk}{e^{\sqrt{k^2 c^2 + c^4} - c^2 - V_{\text{scr}}(r) - \mu/T} + 1},$$

(7)

where c denotes the speed of light in vacuum, k is the momentum of the electron, $k_0(r) = \frac{\sqrt{2V_{\text{scr}}(r)c^2 + V_{\text{scr}}(r)^2}}{c}$, and μ denotes the chemical potential of the plasma.

Once the wave functions have been obtained, the atomic structure is determined and the atomic data such as the radiative transition probability and the photoionization cross section can be obtained for microscopic atomic processes. As an example, the ionization potential of the charge state i is determined by the energy difference between the respective ground levels of charge states i and $i + 1$. The IPD can be obtained by the difference of the ionization potential of the isolated ion and the screened ion embedded in the plasma.

In an LTE plasma at a temperature T, the population of different charge states is determined by the modified Saha equation after considering the NIC effect [48],

$$\frac{N_{i+1} N_e}{N_i} = \frac{b_i Z_e Z_{i+1}}{Z_i} e^{-\frac{\phi_i - \Delta \phi_i}{kT}},$$

(8)

where N_i and Z_i are the population density and partition function of the charge state i, respectively, and N_e the population density of free electrons. The quantity ϕ_i refers to the ionization potential of the charge state i in the isolated ion state and $\Delta \phi_i$ represents the IPD of the charge state i caused by the plasma environment, which can be obtained by a method called the temperature-dependent ion-sphere model [32]. The partition function Z_i of the charge state i is determined by the energy levels of all possible bound quantum states in the dense plasma and their statistical weights, which is obtained by

$$Z_i = \sum_j g_{j,i} e^{-E_{j,i}/kT},$$

(9)

where $E_{j,i}$ and $g_{j,i}$ are the energy and its statistical weight of the quantum state j of the charge state i.

The quantity Z_e is the average partition function of an electron in an ideal classical uniform electron gas, which is expressed as

$$Z_e = 2 \left(\frac{2\pi m_e kT}{h^2} \right)^{3/2},$$

(10)

and $b_i Z_e$ is the partition function of the ionized electrons belonging to the charge state i embedded in a dense plasma

with b_i being determined by

$$b_i = \frac{1}{\int_0^{R_0} 4\pi r^2 dr} \int_0^{R_0} dr \int_0^{\infty} d\epsilon \frac{8\pi}{h^3} (2m)^{\frac{3}{2}} r^2 \epsilon^{\frac{1}{2}}$$

$$\times \frac{1}{e^{\frac{\epsilon + V_i(r)}{kT}} + e^{-\frac{\mu}{kT}}}$$

(11)

to account for the nonhomogeneity, quantum degeneracy, and the interactions among the electrons. In the above expression, the last term $1/(e^{\frac{\epsilon + V_i(r)}{kT}} + e^{-\frac{\mu}{kT}})$ originates from the Fermi-Dirac distribution of free electrons in the LTE plasma, which is degenerated to the classical Boltzmann distribution in the rarified plasma. In such a rarified plasma, the potential $V_i(r)$ is usually assumed to be zero and then the space integration can be separated from that of the momentum with a value which equals to the volume of the ion sphere, i.e., the denominator of the first term in the above expression $\int_0^{R_0} 4\pi r^2 dr$, which leads to the usual Saha equation with $b_i = 1$. This modified Saha equation can be self-consistently solved with the constraint of particle and charge conservation,

$$N = \sum_{il} N_{il},$$

(12)

and the condition of electric neutrality,

$$N_e = \sum_{il} q_i N_{il},$$

(13)

where N is the total population and q_i is the charge of the charge state i.

Once the ionization balance is determined, the emissivity $j(h\nu)$ at a photon energy $h\nu$ can be obtained from the contributions of the bound-bound, the free-bound, and the free-free processes [52],

$$j(h\nu) = j_{bb}(h\nu) + j_{fb}(h\nu) + j_{ff}(h\nu).$$

(14)

The bound-bound emissivity is a summation over all the possible bound-bound transitions,

$$j_{bb}(h\nu) = \sum_k \sum_{j>i} N_{kj} h\nu A_{ji} S_{ji}(h\nu),$$

(15)

where N_{kj} is the population of the level j of the charge state k, A_{ji}, and $S_{ji}(h\nu)$ are the radiative transition probability and the line profile of the transition $j \rightarrow i$, respectively. The profile $S_{ji}(h\nu)$ is taken to be a Voigt function which includes the electron impact, the natural lifetime broadening, and the Doppler broadening. The free-bound part is expressed as

$$j_{fb}(h\nu) = \sum_k \sum_{j,i} N_e N_{kj} h\nu \frac{h\nu - \Delta E}{kT}$$

$$\times \sqrt{\frac{16}{(2\pi m_e kT)}} \sigma_{ji}^r(h\nu - \Delta E) e^{-\frac{(h\nu - \Delta E)}{kT}},$$

(16)

where ΔE is the energy difference between levels i and j, and $\sigma_{ji}^r(h\nu - \Delta E)$ is the radiative recombination cross section. The free-free part is written as

$$j_{ff}(h\nu) = \frac{2\sqrt{2}}{\sqrt{3\pi}} \alpha \sigma_T c N_e \frac{m_e c^2}{kT} g_{ff} e^{-\frac{h\nu}{kT}} \sum_{i=0}^{Z} N_i z_i^2,$$
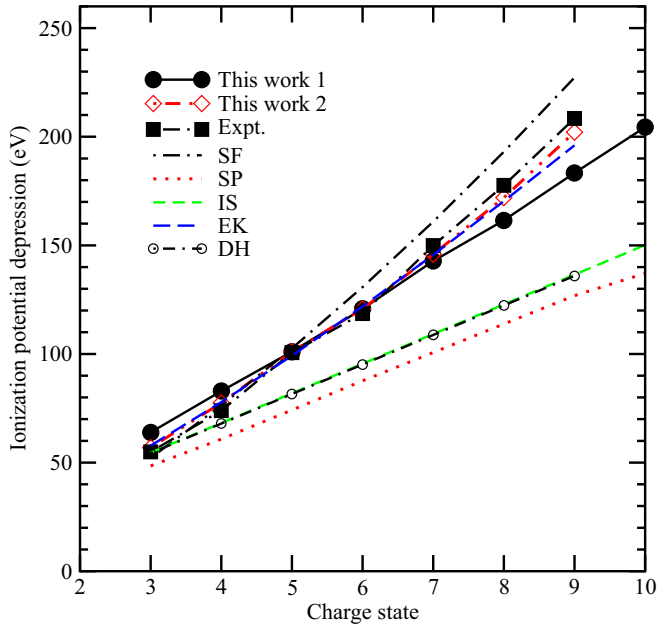
(17)

FIG. 1. Predictions of the IPDs for solid-density Al plasmas by our model (this work 1) are compared with the experimental results (Expt.) [5,6] and other available theoretical models of the dynamical ionic structure factor (SF) [24], the SP [12], the ion-sphere (IS) [53], the EK [13], and the Debye-Hückel (DH) [54] models. The electron temperature is taken to be 200 eV which is obtained from a theoretical simulation [6]. The dashed-dot-diamond line (this work 2) represents our theoretical results using an effective electron temperature of 155, 92, and 45 eV for Al^{7+}, Al^{8+}, and Al^{9+}, respectively.

where α is the fine structure constant, σ_T is the Thomson scattering cross section, g_{ff} is the Gaunt factor, Z is the nuclear charge, N_i is the population number of the charge state i, and z_i is the effective nuclear charge of the charge state i.

III. RESULTS AND DISCUSSION

A. Dense aluminium plasmas

The IPD is a reflection of density effect caused by the screening of the charged particles in the plasmas, which affects the atomic processes such as photoionization and electron impact ionization cross sections of ions embedded in the plasma environment. Advances in experimental technologies including the ultraintensive x-ray free electron lasers and optical lasers make it possible to directly measure the IPD of ions in dense plasmas [5,6,8,9]. As an example, the ultraintensive XFELs is used to heat solid density Al into the dense plasma regime [5,6]. The IPD can be measured by observing the onset of the fluorescence spectroscopy emitted from the K-shell hole and hollow ions. We first investigate the IPDs of ions in solid density Al and then compare them with the experiments [5,6].

Figure 1 compares our theoretically predicted IPDs for a solid density Al plasma at the temperature of 200 eV (the solid circles) with the experimental measurements [5,6]. For further comparison, we also give the theoretical predictions obtained by the other analytical models [12,13,53,54] and by the quantum statistical theory which introduces the ionic dynamical

structure factor (SF) [24]. Experimental studies [5,6] provide information on the IPD within a dense Al plasma using the new generation of intense short-pulse tunable XFELs of the Linac Coherent Light Source [14]. The solid Al is heated into the hot-dense plasma regime by the K-shell photoabsorption and the IPDs are measured by the observation of the K edges from the fluorescence spectroscopy of the various charge states. In the experiments [5,6], the solid Al sample is predicted to be isochorically heated to electron temperatures up to 200 eV under the experimental conditions. The electron temperature is determined by solving the time-dependent rate equations that take into account the processes involved in the interaction between the x-rays and the Al plasma. It can be seen that our predicted IPDs are in good agreement with the experimental values for the lower charge states of Al^{3+}-Al^{6+}, yet they are somewhat smaller than the experimental values for Al^{7+}-Al^{9+} (see black solid line in Fig. 1). Among the other theoretical models, the dynamical ionic SF [24] and the EK models [13] are in better agreement with the measurements than the ion-sphere (IS) [53], the SP [12], and the Debye-Hückel (DH) models.

In what follows, we investigate the possible reasons for the discrepancy between the theoretical predictions and experimental values appearing in the higher charge states of Al^{7+}-Al^{9+}. As is well known, the plasmas produced by the XFELs strongly deviate from the state of thermal dynamic equilibrium [55,56], which means that the free electrons are heated hot while the ions are still cold. Furthermore, the system of free electrons does not exist in the thermal equilibrium during the XFEL irradiation [57], nor is it uniformly distributed around the positively charged ions in space. In such a way the screening of charged particles in the plasma environment on ions is different from that in the LTE plasmas, particularly for the higher charge states which are produced at a later time. In the experiments [5,6], the energy of the laser photons is slightly above the ionization threshold of Al^{9+} and hence the energies of the photoelectrons moving around the ions of Al^{7+}-Al^{9+} produced by the photoionization of the XFEL are much lower than the lowly charge states. Practical simulations on the dynamical evolution of solid density Al plasma show that the higher charge states of Al^{7+}-Al^{9+} are produced at a later time during the XFEL irradiation than the lowly charge states [55–57]. As a result, the free electrons around the ions of Al^{7+}-Al^{9+} are not completely thermalized by the bath of other free electrons and therefore the "effective" (which is defined as the total internal energy per free electron) electron temperature of Al^{7+}-Al^{9+} is lower than the assumed electron temperature obtained in the simulation by the time-dependent rate equations. Moreover, different ions show different electron temperatures during the time evolution. The time-dependent rate equation simulations [55–57] show that the "effective" electron temperature of Al^{7+}-Al^{9+} are 155, 92, and 45 eV, respectively. Using the "effective" electron temperature of Al^{7+}-Al^{9+} instead, the theoretical prediction is in much closer agreement with the experimental values [5,6] (see red diamonds in Fig. 1).

We show in Fig. 2 the predicted IPDs for Al plasmas at the solid density of 2.7 g/cm³ and temperatures of 100, 300, and 600 eV along with the model predictions of the SP [12], the IS [53], the EK [13], and the DH [54] models. At a lower
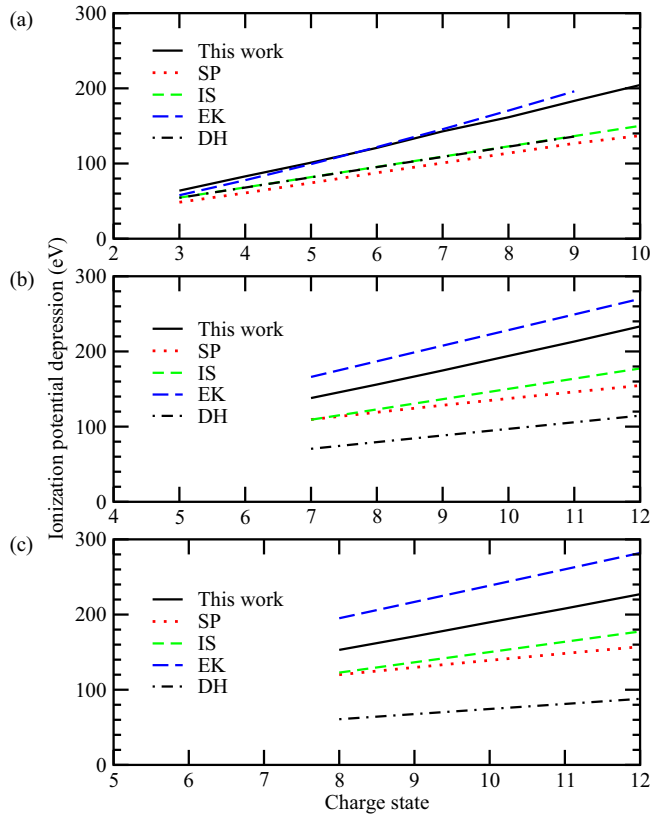
FIG. 2. Ionization potential depressions of Al plasmas at the solid-density of 2.7 g/cm^3 and temperatures of 100 eV (a), 300 eV (b), and 600 eV (c). Predictions by our model are compared with the analytical models of SP [12], the ion-sphere (IS) [53], EK [13], and Debye-Hückel (DH) [54].

FIG. 3. Ionization potential depressions of Al plasmas at the temperature of 200 eV and mass densities of 1.2 g/cm^3 (a), 2.5 g/cm^3 (b), and 4.0 g/cm^3 (c). Predictions by our model are compared with those by the other analytical models, including the SP [12], the IS [53], the EK [13], and the DH [54] models.

temperature of 100 eV, there is a good agreement between our predicted IPDs and those by the EK model, whereas the SP, the IS, and the DH models predict lower IPDs than by the EK and our models. In addition, there is a good agreement for the IPDs predicted by the three models of the SP, the IS, and the DH. With the increase of temperature, the EK model predicts a higher and higher IPD than our theory, yet the DH model predicts a lower and lower IPD. At all cases with different temperatures, there is a general closer agreement between the IPDs predicted by the SP and the IS models.

Figure 3 compares the predicted IPDs obtained by our and other different models for the Al plasmas at the temperature of 200 eV and different mass densities of 1.2, 2.5, and 4.0 g/cm^3. From the inspection of this figure, one can find that the EK model predicts the highest IPDs, whereas the DH model predicts the lowest IPDs for all the studied cases. Our predicted IPDs are smaller than those by the EK model yet larger than those by the SP, the IS, and the DH models. The SP and IS models predict closer IPDs, especially for the lower charge states up to Al^{8+}.

With the increase of plasma temperature and density, the qualitative conclusions drawn from Fig. 3 apply well, as can be seen from Fig. 4, which shows the predicted IPDs at the temperature of 550 eV and different mass densities of 4.0, 5.5, and 9.0 g/cm^3. However, quantitatively and in more details, there is still a difference in the IPDs predicted by the different
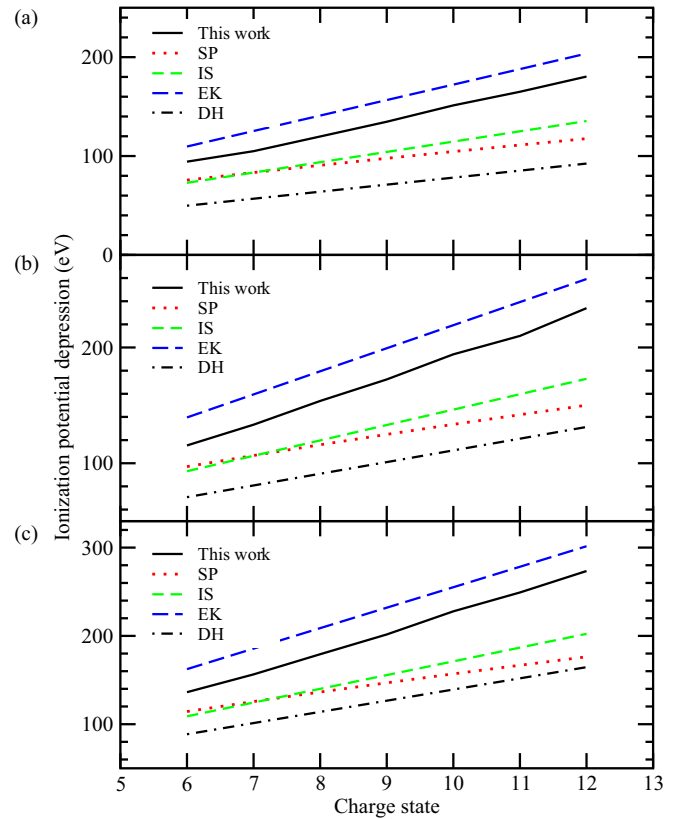
models. For example, the EK model predicts higher IPDs than all other models, and the IPDs obtained by our model are also larger than those by the SP, the IS, and the DH models. In addition, our model predicts slightly smaller IPDs for the Al plasma at the temperature of 500 eV and density of 4.0 g/cm^3 than those at the temperature of 200 eV and density of 4.0 g/cm^3. In such a way, the difference of IPDs predicted by our model and the EK model becomes increasingly larger at the higher plasma temperature for the Al plasma with a same density. Also, it is found that the DH model predicts increasingly lower IPDs at the higher plasma temperature for the Al plasma with the same density.

The physical quantities of the IPDs directly included in the Saha equation do affect the ionization balance of dense plasma. In Fig. 5, we show the charge state distributions (CSDs) of Al plasmas at the solid-density of 2.7 g/cm^3 and temperatures of 100, 300, and 600 eV obtained using the present theory predicted IPDs and those by the analytical models of the SP [12], IS [53], EK [13], and DH [54] models. There is a good agreement in the predicted CSDs by the SP, the IS, and the DH models for all the three cases with different temperatures. This is consistent with the predictions of IPDs by the SP, the IS, and the DH models, as shown in Fig. 2. At the temperatures of 100 and 300 eV, the EK model predicts a much closer CSDs to our results than all the other models. However, with the increase of temperature to up to 600 eV,
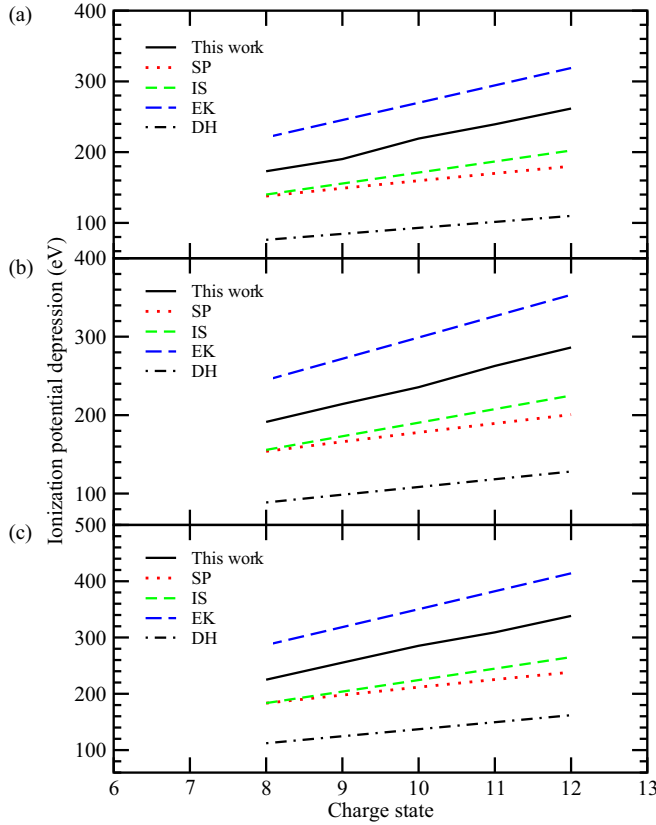
FIG. 4. Ionization potential depressions of Al plasmas at the temperature of 550 eV and mass densities of 4.0 g/cm^3 (a), 5.5 g/cm^3 (b), and 9.0 g/cm^3 (c). Predictions by our model are compared with those by the analytical models of the SP [12], the IS [53], the EK [13], and the DH [54] models.

FIG. 5. Comparison of our predicted charge state distribution of Al plasmas at the solid-density of 2.7 g/cm^3 and temperatures of 100 eV (a), 300 eV (b), and 600 eV (c) with those obtained by the analytical models of the SP [12], the IS [53], the EK [13], and the DH [54] models.

the IS and the SP models predict a much closer CSDs to our results than the other models.

In Fig. 6, we compare the theoretical CSDs of the Al plasmas at a fixed temperature of 200 eV and different mass densities of 1.2, 2.5, and 4.0 g/cm^3 with those obtained by the analytical models of the SP [12], the IS [53], the EK [13], and the DH [54] models. From the inspection to this figure, one can find that the SP, the IS, and the DH models tend to predict a lower average degree of ionization than by the EK and our models. For all the three different mass densities of 1.2, 2.5, and 4.0 g/cm^3, the SP and the IS models predict much closer CSDs than the other models. Such an agreement in the predicted CSDs obtained by the SP and the IS models indicates the consistency of the predicted IPDs by both models (see Fig. 3). At the density of 2.5 g/cm^3, the DH model shows a reasonable agreement with those of the SP [12] and the IS [53] models as well. However, the difference by the DH, the SP, and the IS becomes increasingly larger as the density decreases or increases. Both the EK and our models predict a similar trend of CSDs for all the studied cases.

In Fig. 7, our theoretical CSDs are compared with those by the SF [24], the SP [12], the IS [53], the EK [13], and the DH [54] models for the Al plasmas at a fixed temperature of 550 eV and different mass densities of 4.0, 5.5, and 9.0 g/cm^3. All the theories but the DH one predict the highest
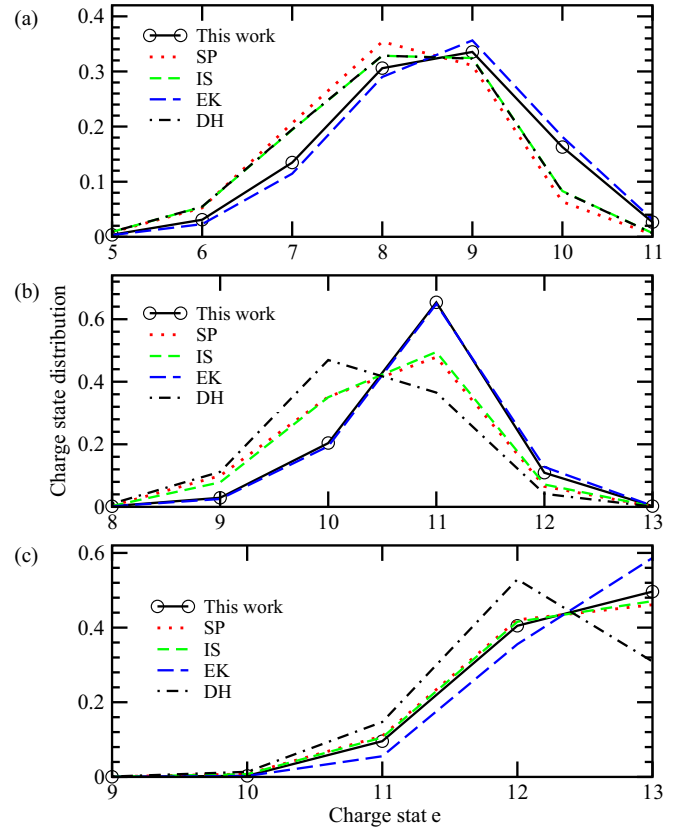
population fraction of hydrogen-like Al^{12+} for all the studied cases, although the plasma mass densities for these studied cases vary greatly. At the highest density of 9.0 g/cm^3, there is an overall reasonable agreement between all the models except for the DH model, which means that the ionization balance in this case is not so model dependent as in the other cases of plasma conditions. Just as shown in Fig. 6, the SP and the IS models predict much closer CSDs than the other models for all the three different mass densities of 4.0, 5.5, and 9.0 g/cm^3. For all the three different densities, the CSDs predicted by the DH model differ considerably from all the others, which is different from that as shown in Fig. 6 at lower densities where there is a reasonable agreement with those predicted by the SP [12] and the IS [53] models at the density of 2.5 g/cm^3. This means that the DH model fails to capture the essential physics with increasing the density and temperature.

Now we consider the NIC effect on the partition functions of the free electrons and on the ionization balance, which has not yet been done in the above discussions. Figure 8 shows the relative partition functions of the free electrons for different charge states of the Al plasmas at temperatures and densities of 550 eV and 1.2 g/cm^3, 650 eV and 2.5 g/cm^3, 700 eV and 4.0 g/cm^3, and 700 eV and 9.0 g/cm^3, respectively. These plasma conditions are taken from those plasmas produced in
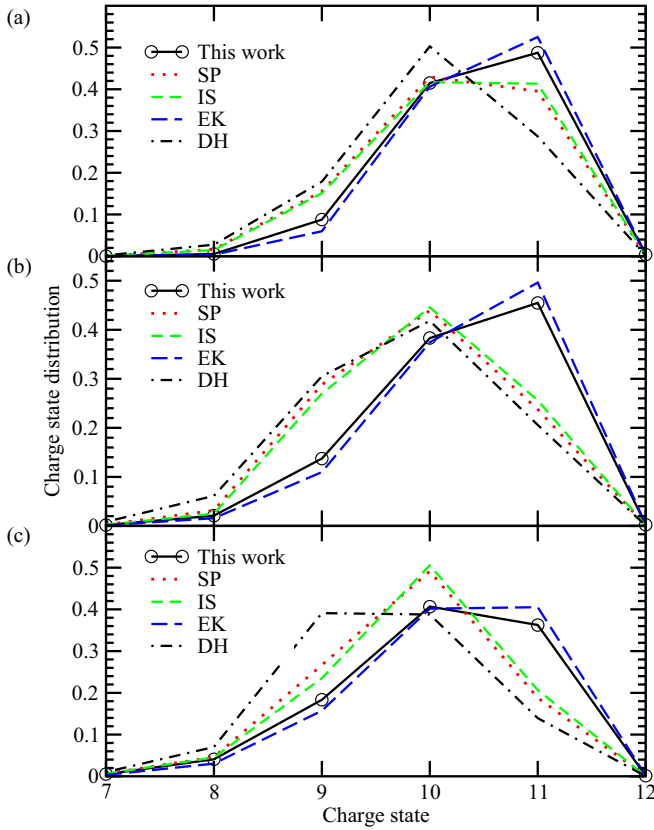
FIG. 6. Comparison of our predicted charge state distribution in the Al plasmas at the temperature of 200 eV and mass densities of 1.2 g/cm^3 (a), 2.5 g/cm^3 (b), and 4.0 g/cm^3 (c) with those obtained by the analytical models of the SP [12], the IS [53], the EK [13], and the DH [54] models.
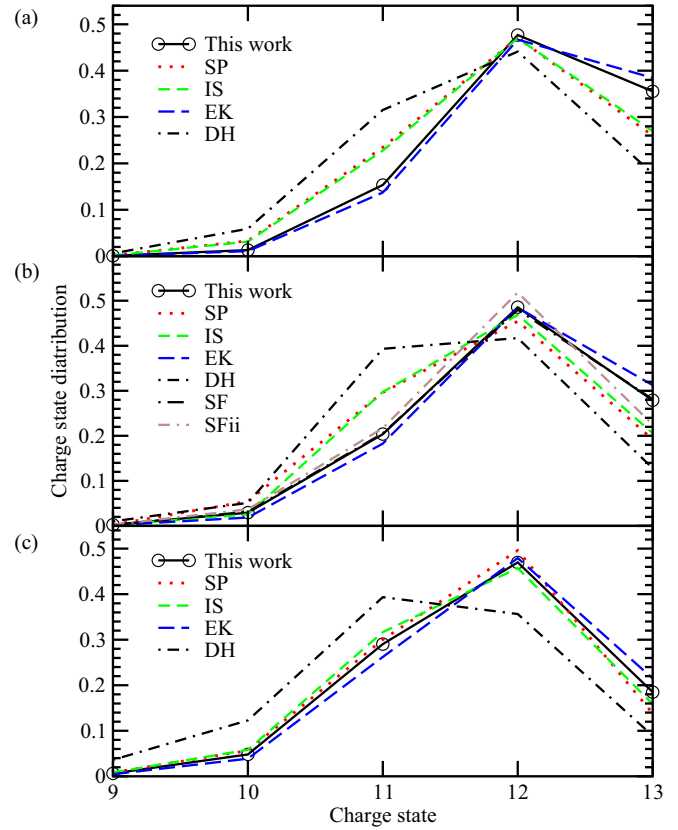

FIG. 7. Comparison of our predicted charge state distribution in the Al plasmas at the temperature of 550 eV and mass densities of 4.0 g/cm^3 (a), 5.5 g/cm^3 (b), and 9.0 g/cm^3 (c) with those obtained by the theoretical models of the SF [24], the SP [12], the IS [53], the EK [13], and the DH [54] models. The black long-dashed line predicted by the SF model is almost completely overlapped by our results, making it nearly invisible in the plot. The label SFii represents the results obtained by the dynamical SF method contributed by the ionic part in the plasma in (b) at 5.5 g/cm^3.

the experiment [8]. Even at such high plasma temperatures, the NIC shows its effect on the relative partition functions of free electrons, which is smaller than unity. With the increase of plasma density, the NIC shows more pronounced effect with smaller relative partition functions of free electrons.

Then we study the NIC effect on the ionization balance. The NIC effect on the CSDs is shown in Fig. 9 for the Al plasmas at temperatures and densities of 650 eV and 2.5 g/cm^3, 700 eV and 4.0 g/cm^3, and 700 eV and 9.0 g/cm^3, respectively. Here the charge state of Al^{13+} refers to the bare ion. At these plasma conditions, the population fraction of the bare ion exceeds more than 30%. With the NIC effect included, the population fractions of the lower charge states become higher than those without including this effect. Moreover, the NIC shows more pronounced effect on the CSDs with increasing the plasma density.

The NIC effect on the ionization balance of plasmas affects the plasma physical properties such as the opacity and the emissivity. In Fig. 10 we compare our theoretical emissivity with the experimental data [8] and the FLYCHK predictions using the SP [12] and the EK [13] models for Al plasmas at different plasma temperature and density conditions of 550 eV and 1.2 g/cm^3, 650 eV and 2.5 g/cm^3, 700 eV and 4.0 g/cm^3, 550 eV and 5.5 g/cm^3, and 700 eV and 9.0 g/cm^3. Both the theoretical and experimental emissivities are in arbitrary units
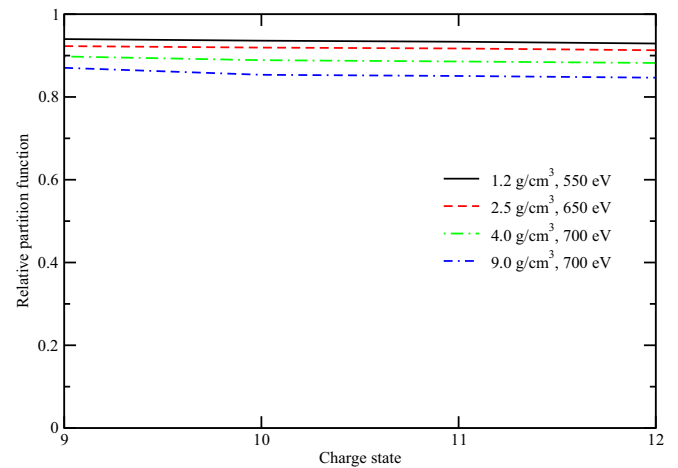

FIG. 8. Relative partition functions b_i of the free electrons for different charge states in following Al plasma conditions of temperatures and densities: [550 eV, 1.2 g/cm^3], [650 eV, 2.5 g/cm^3], [700 eV, 4.0 g/cm^3], and [700 eV, 9.0 g/cm^3]. The relative partition functions of the free electrons are evaluated relative to that of the uniform electron gas [$Z_e = 2(\frac{2\pi m_e kT}{h^2})^{3/2}$] for each respective plasma condition.
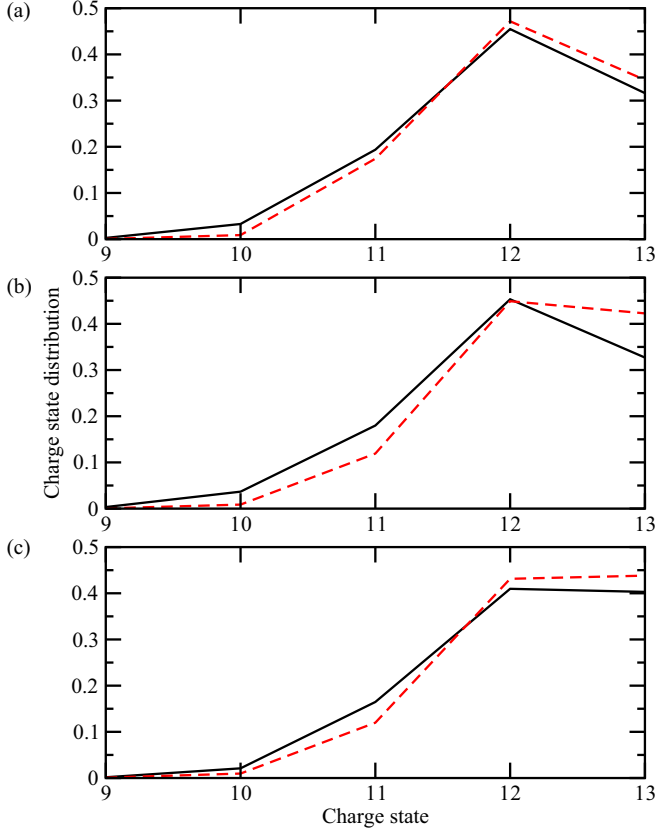
FIG. 9. Comparison of the charge state distribution of Al plasmas with (black solid lines) and without (red dashed lines) considering the NIC effect on the partition functions of free electrons at the following plasma temperature and density conditions: [650 eV, 2.5 g/cm^3] (a), [700 eV, 4.0 g/cm^3] (b), and [700 eV, 9.0 g/cm^3] (c).
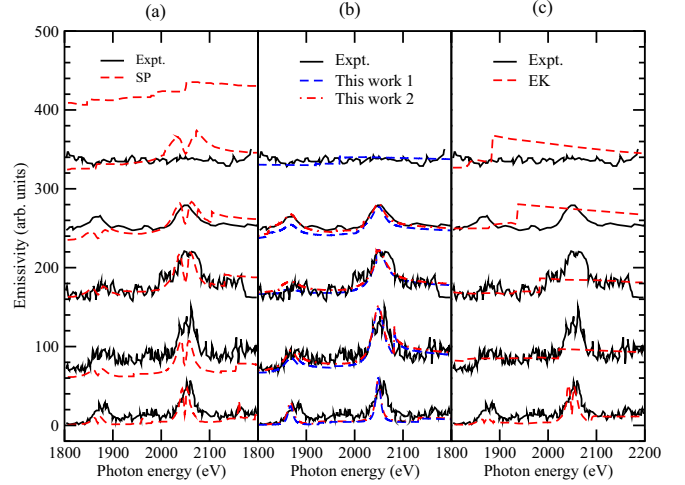

FIG. 10. Comparison of the theoretical emissivity with the experimental data [8] and the FLYCHK predictions using the SP [12] and the EK [13] models for the Al plasmas with (red dashed-dot lines) and without (blue dashed lines) considering the NIC effect on the partition functions of free electrons. The plasma temperature and density conditions are [550 eV, 1.2 g/cm^3], [650 eV, 2.5 g/cm^3], [700 eV, 4.0 g/cm^3], [550 eV, 5.5 g/cm^3], and [700 eV, 9.0 g/cm^3] from the bottom to the top. The SP model has an additional curve at the density of 11.6 g/cm^3.

and have been scaled in intensity for clarity. For plasmas at lower densities of 1.2, 2.5, 4.0, and 5.5 g/cm^3, the emission spectra show two peaks at the photon energies of $\sim$1869 and $\sim$2051 eV, which originate from the radiative transitions of 3p-1s of He-like and H-like Al ions, respectively. From inspecting Fig. 10, it can be seen that our theory is in quantitative agreement with the experiment. Below the density of $\sim$8.0 g/cm^3, the 3p orbital is a bound one, which is consistent with the experimental findings. At the density of 9.0 g/cm^3, both our theory and the experiment indicate that the 3p orbital has become delocalized, that is, changing from the bound orbital at a lower density to the continuum at this density. With including the NIC effect, the quantitative agreement becomes better between our theoretical predictions and the experimental results. The SP prescription for the IPDs are in qualitative agreement with the experiment, yet it predicted that the delocalization of the 3p orbital would not occur until at an even higher density of 11.6 g/cm^3. In contrast, the simulations with the EK model predict a very different outcome, i.e., the delocalization of the 3p orbital will occur at and above the density of 2.5 g/cm^3. Only at the density of 1.2 g/cm^3 the 3p orbital is a bound one.

Regarding the IPD of the dense Al plasmas, it can be seen that the EK model [13] is in better agreement with the

experiment [5] than the SP model [12]. However, the SP model [12] agrees better with the later laser-driven shock experiments [8] than the EK model [13]. Here our scheme and its numerical results reconcile such a contradiction and quantitatively and consistently interpret both experiments. As is well known, the measured emissivity provides a stringent constraint and check on the dense plasma theory including the environment effects. Our proposed theory provides a unified theoretical formalism to treat the environment effects including the plasma screening on the atomic structure, the IPDs, and the ionization balance in the dense Al plasmas.

B. Dense gold plasmas

Now we consider the IPDs and the ionization balance in the dense gold plasmas. In this work, we present the results for Au plasmas at plasma conditions in the mass density range of 1–40 g/cm^3 and the temperature range of 10–2000 eV, which is important for the cases of plasma studies, for example the inertial confinement fusion [4]. Plasmas with large variations in density and temperature can be studied by the present theoretical formalism. Figure 11 shows the IPDs of dense Au plasmas at the temperature of 600 eV and at different mass densities of 10, 20, 30, and 40 g/cm^3. From inspecting this figure, it can be found that a linear relation holds in general for all the cases we studied here with regular density and temperature dependent slopes, and the results show the same characteristics as those by the analytical models [12,13,53,54] as shown for the Al plasmas in Figs. 1– 4. With the increasing of mass density, our calculations show a slight zigzag fluctuations. The higher the density, the stronger the deviation. This reflects a zigzag fluctuation in the plasma screening and the ionization balance. In addition, the conclusion that the IPD
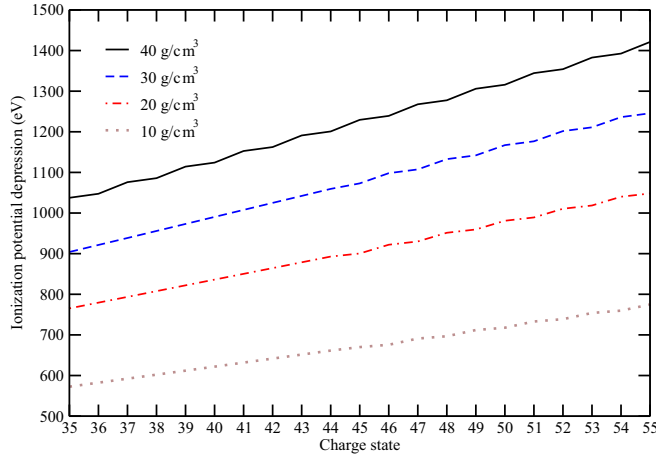
FIG. 11. Ionization potential depression of the dense Au plasmas at the temperature of 600 eV and mass densities of 10, 20, 30, and 40 g/cm^3.

increases with increasing the plasma density still holds as in the case of dense Al plasmas.

Figure 12 shows the IPDs of dense Au plasmas at the temperature of 1000 eV and the same mass densities of 10, 20, 30, and 40 g/cm^3 as those in Fig. 11. While we can draw a similar conclusion as that from Fig. 11, a slight difference from Fig. 11 is in that the zigzag fluctuation is little stronger at the higher temperature. At the temperature of 600 eV as shown in Fig. 11, the dominant charge states are predicted to be from Au^{35+} to Au^{55+}, and the dominant charge states change from Au^{45+} to Au^{60+} at the temperature of 1000 eV, showing that the ionization degrees of the Au plasma become much higher with increasing the plasma temperature from 600 to 1000 eV.

In order to get a more comprehensive understanding towards this phenomenon, in Fig. 13 we show the IPDs of the dense Au plasmas at a wider temperature range of 400–2000 eV. Both the density and the temperature effects can be clearly seen from this plot. For all the cases of different mass
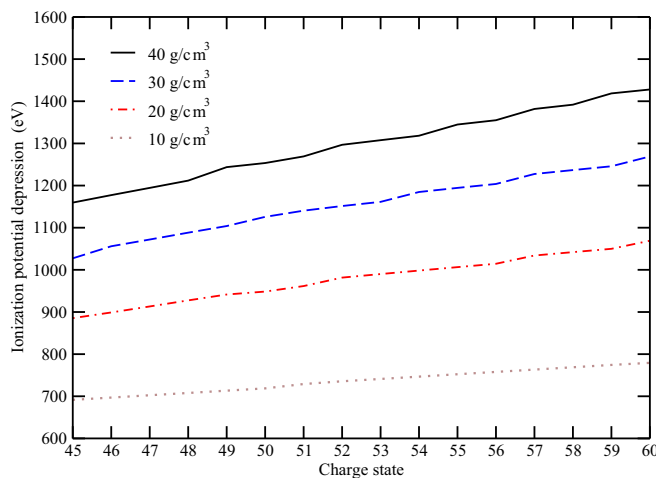

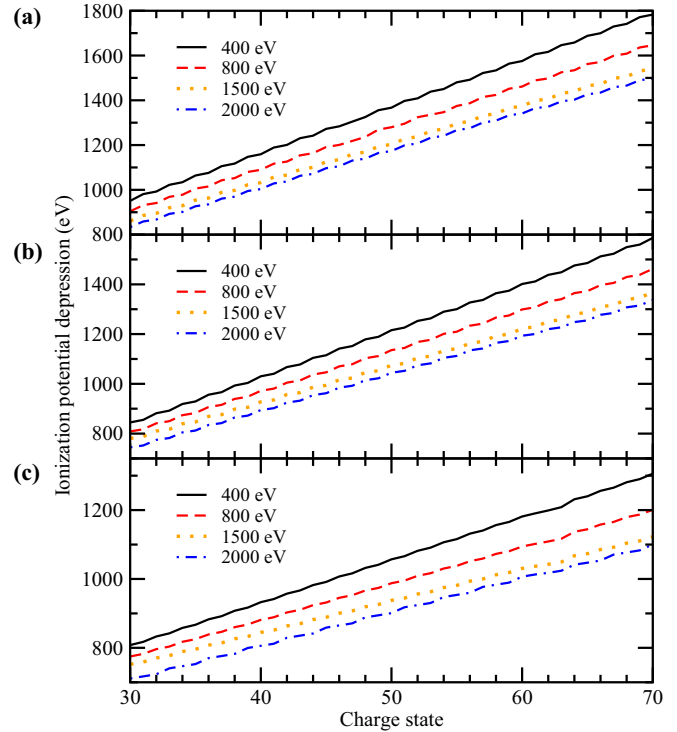FIG. 12. IPD of dense Au plasmas at the temperature of 1000 eV and mass densities of 10, 20, 30, and 40 g/cm^3.

FIG. 13. IPD of dense Au plasmas at temperatures of 400, 800, 1500, and 2000 eV and different mass densities of 40 g/cm^3 (a), 30 g/cm^3 (b), and 20 g/cm^3 (c).

densities, the temperature effect tends to decrease the IPDs with increasing the temperature. And such trend decreases slower with the increasing temperature, and the IPD of a given charge state tends to converge to a definite value at a fixed density.

Now we turn to investigate the NIC effects on the partition functions of the free electrons. As an example, we show in Fig. 14 the density dependence of the partition functions of the free electrons at the temperature of 1000 eV. If the free electrons in the plasma are assumed as uniform electron gas, then the partition functions of the free electrons belonging to different charge states have the same value of $Z_e = 2(\frac{2\pi m_e kT}{h^2})^{3/2}$. To simplify the demonstration of Fig. 14, the partition functions of the free electrons belonging to different charge states are scaled relative to this value. At a given plasma temperature, the relative partition functions of free electrons for different charge states are found to decrease with increasing the mass density. For example, at the density of 10 g/cm^3 and temperature of 1000 eV, the partition function of Au^{55+} is predicted to be 0.889 of that of the uniform electron gas. This relative partition function is decreased to 0.856 at a higher density of 30.0 g/cm^3. In addition, the relative partition functions decrease with increasing the charge states at a given mass density and temperature.

The effect of NIC on the ionization balance is clearly demonstrated in Fig. 15, which shows the population fractions of CSDs for the dense Au plasmas at different mass densities of 5.0, 30.0, and 40.0 g/cm^3 and temperatures of 400, 600, 800, 1000, 1500, and 2000 eV, respectively. As discussed above, since the NIC effect on the energy levels and the IPDs
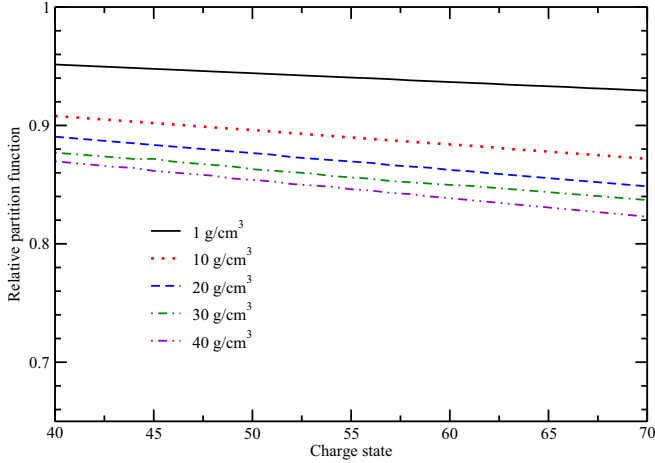
FIG. 14. Relative partition functions (b_i in modified Saha [8]) of the free electrons for different charge states in dense Au plasmas at the temperature of 1000 eV and mass densities of 1.0, 10.0, 20.0, 30.0, and 40.0 g/cm^3, respectively. For each plasma condition, the partition functions are scaled relative to that of the uniform electron gas [$Z_e = 2(\frac{2\pi m_e kT}{h^2})^{3/2}$].
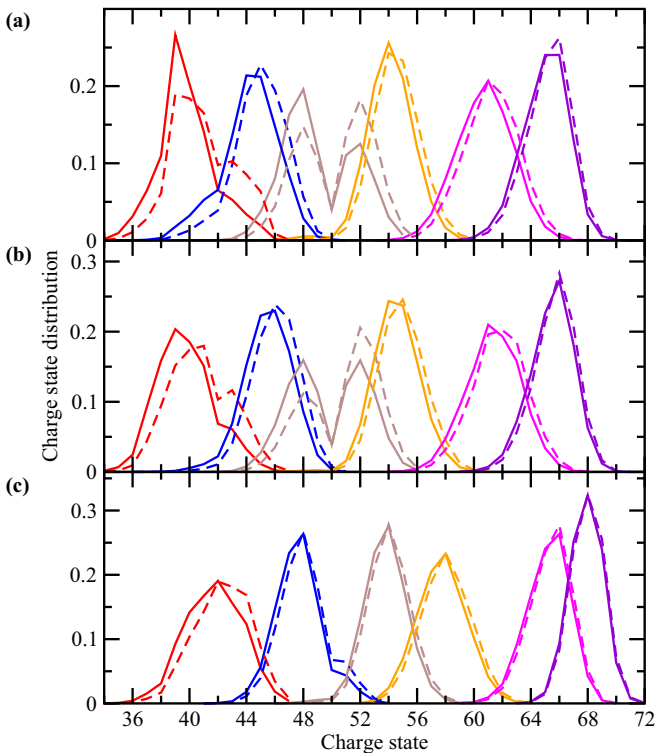

FIG. 15. Comparison of population fractions of the charge state distribution of dense Au plasmas with (solid lines) and without (dashed lines) considering the NIC effect of free electrons on the ionization balance at the mass densities of (a) 40.0 g/cm^3, (b) 30.0 g/cm^3, and (c) 5.0 g/cm^3 and at the temperatures of 400 eV (red solid and dashed lines), 600 eV (blue solid and dashed lines), 800 eV (brown solid and dashed lines), 1000 eV (yellow solid and dashed lines), 1500 eV (lavender solid and dashed lines), and 2000 eV (deep purple solid and dashed lines).

have been considered, the partition functions of ions are the same in the two results with or without including the NIC effect. The only difference is whether the NIC effect on the partition functions of the free electrons is considered or not for the two sets of calculations. If we considered the NIC effect on the partition functions of the free electrons, the predicted CSDs will move to lower charge states compared with those without considering this effect. Generally speaking, the NIC effect on the CSDs is more pronounced at a higher plasma density and lower plasma temperature. In addition, at a given density, the predicted CSDs with or without considering this effect are getting closer and closer with increasing the plasma temperature. For example, at the density of 5.0 g/cm^3 and plasma temperature of above 1500 eV, the difference between the CSDs with or without considering the NIC effect already becomes too small to be observable. However, at a density of 40.0 g/cm^3 and even higher temperature of 2000 eV, the predicted CSDs still show clear difference with or without considering the NIC effect.

From inspecting Fig. 15, a phenomenon of the two-peak structure of the CSDs can be found for both the results with or without considering the NIC effect at the density of 40.0 g/cm^3 and temperature of 800 eV and at 30.0 g/cm^3 and 800 eV. As is well known, the CSDs of low-density plasmas generally show a single-peak distribution. For dense plasmas, however, the two-peak structure of the CSDs can be found at some plasma conditions. The two local maxima are found to be for the populations of Au^{48+} and Au^{52+}. For both plasma conditions at the densities of 40.0 and 30.0 g/cm^3, the two-peak structure of the CSDs shows a local minimum for the population fractions of Au^{50+}, meaning that the higher (Au^{52+}) and the lower (Au^{48+}) charge states have larger populations than Au^{50+}.

The two-peak structure is not observed at the mass density of 5.0 g/cm^3 in Fig. 15. As a matter of fact, this phenomenon of the two-peak structure of the CSDs indeed happened at this density, as shown in Fig. 16 at finer temperature resolutions from 600 to 800 eV. From this plot, we can see that the two-peak structure of the CSDs exists in the plasma temperature range of 600–800 eV. Here and in what follows, the NIC effects have been considered in the determination of the ionization balance.

We suggest that the two-peak structure of the CSDs should be a common phenomenon for dense plasmas, particularly for mid-Z and high-Z plasmas. This phenomenon for mid-Z iron plasmas has been demonstrated in a previous publication [48]. Using this framework [48], we resolved the controversy of the two experiments on aluminum plasmas [5,8], as demonstrated in the previous subsection. Furthermore, the different features of the two-peak structure of the CSDs in high-Z plasmas from the mid-Z plasmas are revealed in this work to have a more complete understanding on the ionization balance of dense plasmas. In addition, three-peak distribution of the CSDs in LTE plasmas is predicted for the first time, to the best of our knowledge.

In Fig. 17, we give the population fractions of different charge states of Au plasmas at a density of 40.0 g/cm^3 and different temperatures ranging from 150 to 1100 eV. At the density of 40.0 g/cm^3, it can be found that there exist three temperature ranges in which the CSDs show the two- or even
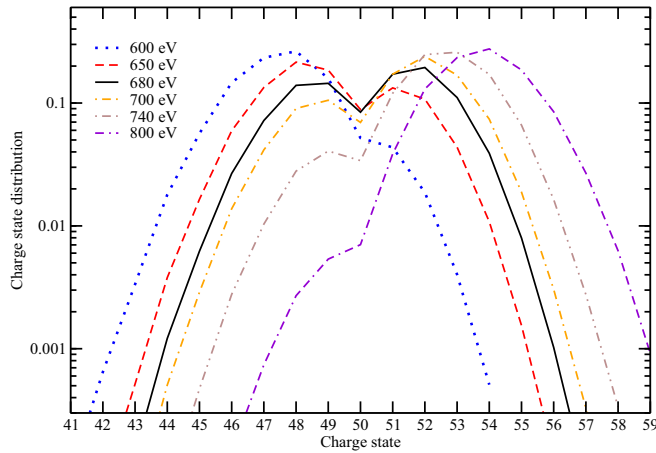
FIG. 16. The two-peak structure of dense Au plasmas at the density of 5.0 g/cm^3 and different temperatures. The population fractions of the CSDs are given at the temperatures of 600, 650, 680, 700, 740, and 800 eV, at which plasma conditions the phenomenon of the two-peak structure can be found. The NIC effects have been considered in the determination of the ionization balance.

three-peak structure. The first temperature range is located from 150 to 320 eV, where the three-peak structure and the two-peak structure coexist simultaneously. At a lower temperature range of ~150-290 eV, the CSDs show the three-peak structure with three maxima in population fractions. As an example, at the temperature of 200 eV, the three peak values of the population fractions are found for the charge states of Au^{26+}, Au^{29+}, and Au^{32+}. At a little higher temperature of 230 eV, the three peak values of the population fractions are found for the charge states of Au^{27+}, Au^{29+}, and Au^{32+}. The maximum of the charge state in the first peak is shifted from Au^{26+} at the temperature of 200 eV to Au^{27+} at the temperature of 230 eV. With further increasing the temperature to 255 eV, the peak of the lowest charge state begins to disappear and then the three-peak structure starts to change into the two-peak structure for the CSDs. One specific temperature range is from ~255 to 320 eV, in which the two-peak structure is found for the CSDs. The second specific temperature range is found from ~400 to ~570 eV, in which the two-peak structure exists, but at the two end temperatures of 400 and 570 eV, the CSDs show a normal single-peak population distribution. The third specific temperature range is predicted to be located at ~670-1070 eV, in which the two-peak structure is also observed, just as that in the second temperature range. Based on the above discussions, the two-peak and the three-peak structures appear in a wide temperature range, which can be safely termed as a common phenomenon for the population distribution among the different charge states of dense heavy-Z plasmas. In addition, our results show that the two- and the three-peak structures for the CSDs also occur in a wider regime of density and temperature for heavier-than Au plasmas than for lighter Fe plasmas [48]. In heavy-Z plasmas, there are more electronic subshells and a wider distribution of the charge states than those in lighter element plasmas, which is the main reason for this new feature.

The reason for the occurrence of the two- and the three-peak structures for the CSDs works similarly for the dense
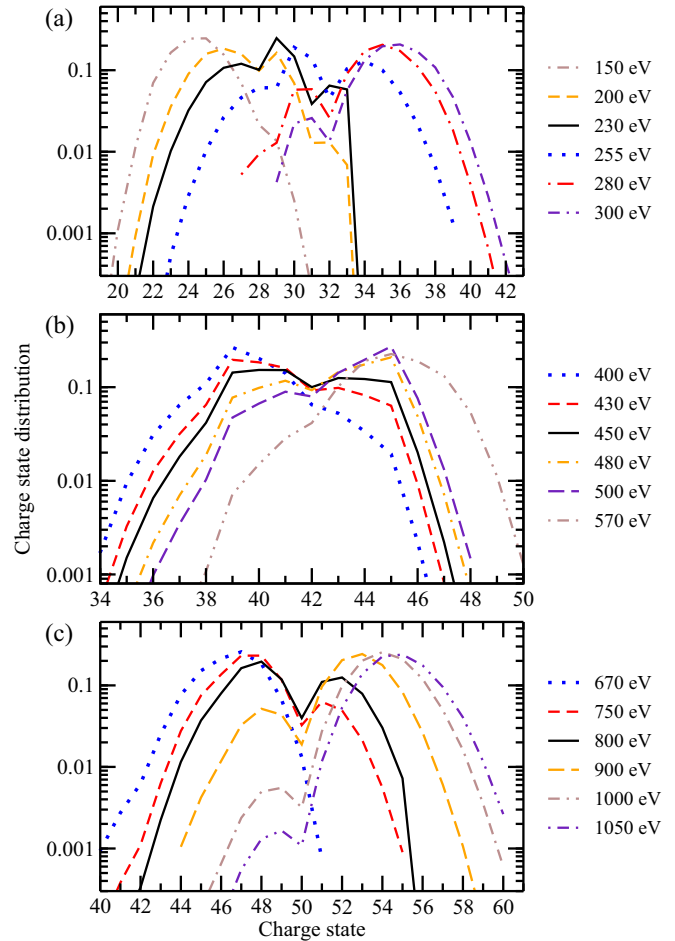

FIG. 17. The two- and three-peak structures of dense Au plasmas plasma at the density of 40.0 g/cm^3 and different temperatures. The population fractions of different charge states are given at the temperatures of 150, 200, 230, 255, 280, and 300 eV (a); 400, 430, 450, 480, 500, and 570 eV (b); and 670, 750, 800, 900, and 1000 eV (c). At these plasma conditions the phenomenon of the two-peak structure can be found in a wide temperature range. The NIC effects have been considered in the determination of the ionization balance.

Au plasmas. Now we take the two-peak distribution observed in the third temperature range of ~670-1070 eV [see Fig. 17(c)] as an example to illustrate this matter. From inspecting Fig. 17(c), one finds that the local minimum value of the populations originates from the charge state of Au^{50+}. For lower charge states than the ion of Au^{50+}, their ground configuration $1s^2 2s^2 2p^6 3s^2 3p^6 3d^{10} 4l^m$ ($m = 1, 2, \dots$) has $4l$ ($l = 0, 1,$ and 2) outmost electrons. However, the ion of higher charge states than Au^{50+} has a ground configuration of $1s^2 2s^2 2p^6 3s^2 3p^6 3d^n$ ($n = 10, 9, 8, \dots, 1, 0$), which does not have any $4l$ electronic subshell. Because of the difference in the principal quantum number of the outmost electrons (lower charge states $n = 4$ and higher charge states $n = 3$), the ionization potentials (after considering the IPD effect) of the higher charge states than Au^{50+} are much higher than those of the lower charge states than the ion of Au^{50+} (see Table I for the corresponding data at the density of 40.0 g/cm^3 and temperature of 800 eV). At a lower plasma temperature than 670 eV, the thermal ionization cannot effectively ionize the

TABLE I. The ionization potentials (IPs) and the partition functions (PFs) of different Au ions from Au^{40+} to Au^{60+} embedded in the Au plasma at the density of 40.0 g/cm^3 and temperature of 800 eV. The plasma screening effect on the IPDs have been considered in the ionization potentials of different charge states.

Charge state	IP (eV)	PF
Au^{40+}	838.09	36670.4
Au^{41+}	879.43	22850.4
Au^{42+}	909.43	11980.8
Au^{43+}	1129.99	13090.9
Au^{44+}	1171.12	14491.8
Au^{45+}	1202.25	10576.2
Au^{46+}	1244.69	5361.6
Au^{47+}	1422.36	2729.5
Au^{48+}	1470.79	1024.6
Au^{49+}	1604.64	205.8
Au^{50+}	1658.72	27.2
Au^{51+}	3574.01	31.9
Au^{52+}	3679.83	167.6
Au^{53+}	3811.62	562.0
Au^{54+}	3953.17	1346.0
Au^{55+}	4071.33	2409.3
Au^{56+}	4188.09	3358.3
Au^{57+}	4420.87	3974.2
Au^{58+}	4549.10	4627.2
Au^{59+}	4691.21	4239.4
Au^{60+}	4821.38	3435.4

higher charge states than Au^{50+} and hence the CSDs show the normal single peak distribution. With the increase of the plasma temperature, the thermal ionization starts to effectively ionize the higher charge states than Au^{50+} and hence the double peak distribution of the ion populations begins to appear. For the higher charge states than Au^{50+}, the variation of the quantity of $b_i Z_e e^{-\frac{\phi_i - \Delta\phi_i}{kT}}$ with increasing the charge state is much less than the variation of the internal partition functions of ions contributed by the bound electrons (see Table I). Figure 14 shows that the variation of b_i with increasing the charge states is a slow-varying quantity. Furthermore, the ionization potentials of the ions higher than Au^{50+} are relatively close and thus the factor $e^{-\frac{\phi_i - \Delta\phi_i}{kT}}$ is also a slow varying function of the charge states except from Au^{50+} to Au^{51+}. As a result, the CSDs are dominated by the ratio of partition function Z_{i+1}/Z_i which varies relatively faster with increasing the charge state than the factor of $b_i Z_e e^{-\frac{\phi_i - \Delta\phi_i}{kT}}$ in the modified Saha equation. In such a way, the appearance of the two-peak distribution of the CSDs shifts from a lower temperature to a higher temperature. With further increasing the plasma temperature to up to ~1100 eV, the thermal ionization can now effectively ionize the higher charge states than Au^{50+} and thus the population fractions of the lower charge states than Au^{50+} start to become trivial or negligible. When the two-peak structure disappears, the CSDs return to the normal single-peak distribution.

Finally, we discuss the average degree of ionization obtained by the ionization balance equation. In Fig. 18, we show the average degree of ionization of the dense Au plasmas as a function of the plasma temperature at the mass
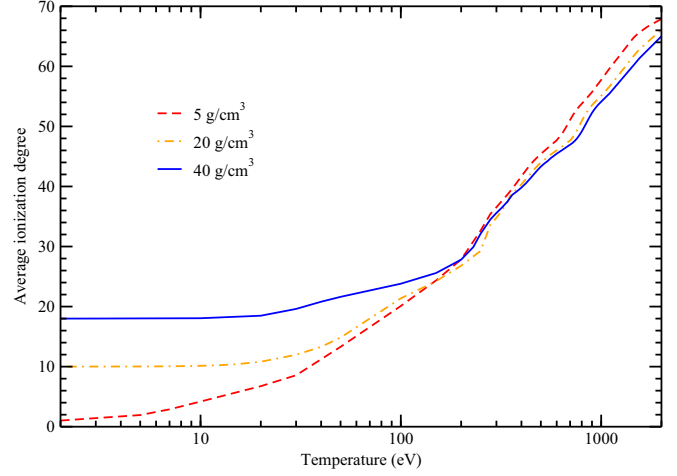

FIG. 18. Average degree of ionization of Au plasmas as a function of plasma temperature at mass densities of 5.0, 20.0 and 40.0 g/cm^3. The NIC effects have been considered in the determination of ionization balance.

densities of 5.0, 20.0, and 40.0 g/cm^3. At all these densities, the plasma undergoes similar ionization phases, i.e., at a lower temperature the pressure ionization plays a dominant role in the ionization balance, and at a much higher temperature the thermal ionization dominates the ionization process. Between these two temperature ranges, the pressure ionization and the thermal ionization compete with each other. For example, at the density of 40.0 g/cm^3, the pressure ionization dominates the ionization equilibrium for the temperature up to ~20 eV, and then the pressure ionization and the thermal ionization compete with each other for the temperature range from ~20 eV to ~200 eV, and above ~200 eV, the thermal ionization dominates the ionization process. From inspecting Fig. 18, one can see that the average degree of ionization shows a continuous variation over the whole temperature range from ~2 to ~2000 eV at all the mass densities of 5.0, 20.0, and 40.0 g/cm^3. Actually, a thermodynamic consistency is ensured with the Maxwell's equations using the theoretical formalism [40] to avoid the thermodynamic inconsistency of the Saha equation [58].

Understanding the ionization balance of dense plasmas will help to study its physical properties such as solving for the plasma opacity [59–72] and the equation of states. The features shown in the dense Au plasmas discussed in this work will usually affect the accurate determination of the radiative properties [73–79], the electrical conductivity [80], the electron transport coefficients [81], and other related physical quantities. The theoretical method presented here provides more accurate treatment on the ionization balance and the charge state distribution and therefore constitutes a basis for further investigations on the dense plasmas. It will also help the diagnostics on dense plasma parameters [82].

IV. CONCLUSION

In summary, we have investigated the nonideal effects on the ionization potential depression and the ionization balance in dense Al and Au plasmas. Based on a local-density

temperature-dependent ion-sphere model, a unified and self-consistent theoretical formalism is developed to calculate the ionization potential depression and all the other physical quantities included in the modified Saha equation, including the partition functions of ions of different charge states and the free electrons. The plasma screening effects on the ionization potential depression and on the partition functions of both ions of different charge states and the free electrons are considered self-consistently in the model. In addition, the usual assumption of uniform free electrons in the standard Saha equation is no longer required by introducing the realistic spatial distribution of the free electrons in the plasmas. At the limit of low plasma density and high temperature, the present theoretical formalism naturally simplifies to the usual standard ionization balance equation. For dense plasmas, the pressure ionization dominates the ionization balance at the lower plasma temperature and the thermal ionization dominates at the higher plasma temperature. In between these two cases, the pressure ionization competes with the thermal ionization, which complicates the study of the ionization balance. An accurate description of the pressure ionization is important at the lower and medium plasma temperature where the pressure ionization plays a major role in determining the charge state distribution. This study shows that the unified and self-consistent treatment on the ionization balance is necessary to obtain more accurate charge state distributions.

For Al plasmas, recent experimental studies show that the currently widely used analytical models cannot satisfactorily explain the two published experimental measurements on the ionization potential depression. Here, by using the local-density temperature-dependent ion-sphere model, we successfully interpreted both experiments on the measurement of the ionization potential depression, where one experiment can be better explained by the Stewart-Pyatt model while the other agrees better with the Ecker-Kröll model. For heavy Au plasmas, researches indicate that the two-peak structure of the charge state distribution is common for dense plasmas above the density of $\sim 1\,\mathrm{g/cm^3}$. With the increase of plasma density, the appearance of the three-peak structure is predicted by the present theoretical formalism. In particular, it is found that both the two-peak and the three-peak structures appear simultaneously for denser Au plasmas at a density of $40\,\mathrm{g/cm^3}$. The reason for the occurrence of the two-peak and the three-peak structures for the CSDs is demonstrated in detail for the dense Au plasmas by continuously increasing the plasma temperature. The two-peak and the three-peak structures for the CSDs are found to occur mainly below or above some certain ion charge states with a closed-shell electron structure of the ground configuration and thus having a much larger ionization potential and a minimum partition function value than the other ion charge states.

[1] A. L. Kritcher, C. S. Damian, T. Döppner, B. Bachmann, L. X. Benedict, G. W. Collins, J. L. DuBois, F. Elsner, G. Fontaine, J. A. Gaffney *et al.*, A measurement of the equation of state of carbon envelopes of white dwarfs, Nature (London) **584**, 51 (2020).

[2] N. Giammichele, S. Charpinet, G. Fontaine, E. M. Green, V. Van Grootel, W. Zong, and M. A. Dupret, A large oxygen-dominated core from the seismic cartography of a pulsating white dwarf, Nature (London) **554**, 73 (2018).

[3] H. Abu-Shawareb, R. Acree, P. Adams *et al.* (Indirect Drive ICF Collaboration), Lawson criterion for ignition exceeded in an inertial fusion experiment, Phys. Rev. Lett. **129**, 075001 (2022).

[4] O. A. Hurricane, P. K. Patel, R. Betti, D. H. Froula, S. P. Regan, S. A. Slutz, M. R. Gomez, and M. A. Sweeney, Physics principles of inertial confinement fusion and U.S. program overview, Rev. Mod. Phys. **95**, 025005 (2023).

[5] O. Ciricosta, S. M. Vinko, H. K. Chung, B. I. Cho, C. R. D. Brown, T. Burian, J. Chalupsky, K. Engelhorn, R. W. Falcone, C. Graves *et al.*, Direct measurements of the ionization potential depression in a dense plasma, Phys. Rev. Lett. **109**, 065002 (2012).

[6] O. Ciricosta, S. M. Vinko, B. Barbrel, D. S. Rackstraw, T. R. Preston, T. Burian, J. Chalupský, B. I. Cho, H.-K. Chung, G. L. Dakovski *et al.*, Measurements of continuum lowering in solid-density plasmas created from elements and compounds, Nat. Commun. **7**, 11713 (2016).

[7] E. A. Seddon, J. A. Clarke, D. J. Dunning, C. Masciovecchio, C. J. Milne, F. Parmigiani, D. Rugg, J. C. H. Spence, N. R. Thompson, K. Ueda, S. M. Vinko, J. S. Wark, and W. Wurth, Short-wavelength free-electron laser sources and science: A review, Rep. Prog. Phys. **80**, 115901 (2017).

[8] D. J. Hoarty, P. Allan, S. F. James, C. R. D. Brown, L. M. R. Hobbs, M. P. Hill, J. W. O. Harris, J. Morton, M. G. Brookes, R. Shepherd *et al.*, Observations of the effect of ionization-potential depression in hot dense plasma, Phys. Rev. Lett. **110**, 265003 (2013).

[9] L. B. Fletcher, A. L. Kritcher, A. Pak, T. Ma, T. Doppner, C. Fortmann, L. Divol, O. S. Jones, O. L. Landen, H. A. Scott, J. Vorberger, D. A. Chapman, D. O. Gericke, B. A. Mattern, G. T. Seidler, G. Gregori, R. W. Falcone, and S. H. Glenzer, Observations of continuum depression in warm dense matter with X-Ray Thomson scattering, Phys. Rev. Lett. **112**, 145004 (2014).

[10] D. Kraus, D. A. Chapman, A. L. Kritcher, R. A. Baggott, B. Bachmann, G. W. Collins, S. H. Glenzer, J. A. Hawreliak, D. H. Kalantar, O. L. Landen *et al.*, X-ray scattering measurements on imploding CH spheres at the National Ignition Facility, Phys. Rev. E **94**, 011202(R) (2016).

[11] T. Döppner, M. Bethkenhagen, D. Kraus, P. Neumayer, D. A. Chapman, B. Bachmann, R. A. Baggott, M. P. Bohme, L. Divol, and R. W. Falcone, Observing the onset of pressure-driven K-shell delocalization, Nature (London) **618**, 270 (2023).

[12] J. C. Stewart and K. D. Pyatt, Lowering of ionization potentials in plasmas, Astrophys. J. **144**, 1203 (1966).

[13] G. Ecker and W. Kröll, Lowering of the ionization energy for a plasma in thermodynamic equilibrium, Phys. Fluids **6**, 62 (1963).

[14] P. Emma, R. Akre, J. Arthur, R. Bionta, C. Bostedt, J. Bozek, A. Brachmann, P. Bucksbaum, R. Coffee, F.-J. Decker *et al.*, First lasing and operation of an ångstrom-wavelength free-electron laser, Nat. Photon. **4**, 641 (2010).

[15] T. R. Preston, S. M. Vinko, O. Ciricosta, H. K. Chung, R. W. Lee, and J. S. Wark, The effects of ionization potential depression on the spectra emitted by hot dense aluminium plasmas, High Energy Density Phys. **9**, 258 (2013).

[16] S.-K. Son, R. Thiele, Z. Jurek, B. Ziaja, and R. Santra, Quantum-mechanical calculation of ionization-potential lowering in dense plasmas, Phys. Rev. X **4**, 031004 (2014).

[17] C. A. Iglesias, A plea for a reexamination of ionization potential depression measurements, High Energy Density Phys. **12**, 5 (2014).

[18] S. B. Hansen, J. Colgan, A. Y. Faenov, J. Abdallah, Jr., S. A. Pikuz, Jr., I. Yu. Skobelev, E. Wagenaars, N. Booth, O. Culfa, R. J. Dance *et al.*, Detailed analysis of hollow ions spectra from dense matter pumped by X-ray emission of relativistic laser plasma, Phys. Plasmas **21**, 031213 (2014).

[19] B. J. B. Crowley, Continuum lowering—A new perspective, High Energy Density Phys. **13**, 84 (2014).

[20] A. Calisti, S. Ferri, and B. Talin, Ionization potential depression for non equilibrated aluminum plasmas, J. Phys. B: At. Mol. Opt. Phys. **48**, 224003 (2015).

[21] S. M. Vinko, O. Ciricosta, and J. S. Wark, Density functional theory calculations of continuum lowering in strongly coupled plasmas, Nat. Commun. **5**, 3533 (2014).

[22] S. X. Hu, Continuum lowering and Fermi-surface rising in strongly coupled and degenerate plasmas, Phys. Rev. Lett. **119**, 065001 (2017).

[23] M. Stransky, Monte Carlo simulations of ionization potential depression in dense plasmas, Phys. Plasmas **23**, 012708 (2016).

[24] C. L. Lin, G. Röpke, W. D. Kraeft, and H. Reinholz, Ionization-potential depression and dynamical structure factor in dense plasmas, Phys. Rev. E **96**, 013202 (2017).

[25] F. B. Rosmej, Ionization potential depression in an atomi-solid-plasma picture, J. Phys. B: At. Mol. Opt. Phys. **51**, 09LT01 (2018).

[26] M. F. Kasim, J. S. Wark, and S. M. Vinko, Validating continuum lowering models via multi-wavelength measurements of integrated X-ray emission, Sci. Rep. **8**, 6276 (2018).

[27] A. Ali, G. S. Naz, M. S. Shahzad, R. Kouser, Aman-ur-Rehman, and M. H. Nasim, Improved continuum lowering calculations in screened hydrogenic model with l-splitting for high energy density systems, High Energy Density Phys. **26**, 48 (2018).

[28] G. Röpke, D. Blaschke, T. Döppner, C. L. Lin, W. D. Kraeft, R. Redmer, and H. Reinholz, Ionization potential depression and Pauli blocking in degenerate plasmas at extreme densities, Phys. Rev. E **99**, 033201 (2019).

[29] C. L. Lin, Quantum statistical approach for ionization potential depression in multi-component dense plasmas, Phys. Plasmas **26**, 122707 (2019).

[30] J. L. Zeng, Y. J. Li, C. Gao, and J. M. Yuan, Screening potential and continuum lowering in a dense plasma under solar-interior conditions, Astron. Astrophys. **634**, A117 (2020).

[31] J. L. Zeng, Y. J. Li, Y. Hou, and J. M. Yuan, Ionization potential depression and ionization balance in dense carbon plasma under solar and stellar interior conditions, Astron. Astrophys. **644**, A92 (2020).

[32] J. L. Zeng, C. Ye, Y. J. Li, and J. M. Yuan, Ionization potential depression in dense iron plasmas near solid density, Results Phys. **40**, 105836 (2022).

[33] F. J. Rogers, F. J. Swenson, and C. A. Iglesias, OPAL equation-of-state tables for astrophysical applications, Astrophys. J. **456**, 902 (1996).

[34] S. X. Hu, D. T. Bishel, D. A. Chin, P. M. Nilson, V. V. Karasiev, I. E. Golovkin, M. Gu, S. B. Hansen, D. I. Mihaylov, N. R. Shaffer *et al.*, Probing atomic physics at ultrahigh pressure using laser-driven implosions, Nat. Commun. **13**, 6780 (2022).

[35] H. M. Johns, R. C. Mancini, P. Hakel, T. Nagayama, V. A. Smalyuk, S. P. Regan, and J. Delettrez, Compressed shell conditions extracted from spectroscopic analysis of Ti K-shell absorption spectra with evaluation of line self-emission, Phys. Plasmas **21**, 082711 (2014).

[36] S. B. Hansen, E. C. Harding, P. F. Knapp, M. R. Gomez, T. Nagayama, and J. E. Bailey, Changes in the electronic structure of highly compressed iron revealed by X-ray fluorescence lines and absorption edges, High Energy Density Phys. **24**, 39 (2017).

[37] L. A. Pickworth, B. A. Hammel, V. A. Smalyuk, A. G. MacPhee, H. A. Scott, H. F. Robey, O. L. Landen, M. A. Barrios, S. P. Regan, M. B. Schneider *et al.*, Measurement of hydrodynamic growth near peak velocity in an inertial confinement fusion capsule implosion using a self-radiography technique, Phys. Rev. Lett. **117**, 035001 (2016).

[38] D. T. Bishel, P. M. Nilson, D. A. Chin, J. J. Ruby, E. Smith, S. X. Hu, R. Epstein, I. E. Golovkin, J. R. Rygg, and G. W. Collins, Toward constraint of ionization-potential depression models in a convergent geometry, High Energy Density Phys. **50**, 101076 (2024).

[39] S. X. Hu, V. V. Karasiev, V. Recoules, P. M. Nilson, N. Brouwer, and M. Torrent, Interspecies radiative transition in warm and superdense plasma mixtures, Nat. Commun. **11**, 1989 (2020).

[40] D. Mihalas, W. Däppen, and D. Hummer, The equation of state for stellar envelopes. II. Algorithm and selected results, Astrophys. J. **331**, 815 (1988).

[41] D. Saumon and G. Chabrier, Fluid hydrogen at high density: Pressure dissociation, Phys. Rev. A **44**, 5122 (1991).

[42] A. Y. Potekhin, G. Massacrier, and G. Chabrier, Equation of state for partially ionized carbon at high temperatures, Phys. Rev. E **72**, 046402 (2005).

[43] M. R. Zaghloul, Integrability criterion for lowering of ionization potentials and formulation of the solution of the inverse problem of constructing consistent thermodynamic functions of nonideal plasmas, Phys. Rev. E **79**, 016410 (2009).

[44] Y. V. Arkhipov, F. B. Baimbetov, and A. E. Davletov, Ionization equilibrium and equation of state of partially ionized hydrogen plasmas: Pseudopotential approach in chemical picture, Phys. Plasmas **12**, 082701 (2005).

[45] K. Wang, Z. Shi, Y. Shi, J. Bai, J. Wu, and S. Jia, The equation of state and ionization equilibrium of dense aluminum plasma with conductivity verification, Phys. Plasmas **22**, 062709 (2015).

[46] T. S. Ramazanov, M. T. Gabdullin, K. N. Dzhumagulova, and R. Redmer, Ionization equilibrium and composition of a dense partially ionized metal plasma, Contrib. Plasma Phys. **51**, 391 (2011).

[47] I. Shimamura and T. Fujimoto, State densities and ionization equilibrium of atoms in dense plasmas, Phys. Rev. A **42**, 2346 (1990).

[48] J. L. Zeng, Y. J. Li, Y. Hou, and J. M. Yuan, Nonideal effect of free electrons on ionization equilibrium and radiative property in dense plasmas, Phys. Rev. E **107**, L033201 (2023).

[49] P. Jönsson, X. He, C. F. Fischer, and I. Grant, The grasp2K relativistic atomic structure package, Comput. Phys. Commun. **177**, 597 (2007).

[50] M. F. Gu, The flexible atomic code, Can. J. Phys. **86**, 675 (2008).

[51] Y. Q. Li, J. H. Wu, Y. Hou, and J. M. Yuan, Influence of hot and dense plasmas on energy levels and oscillator strengths of ions: Beryllium-like ions for $Z = 26-36$, J. Phys. B **41**, 145002 (2008).

[52] C. Gao, J. L. Zeng, Y. Q. Li, F. T. Jin, and J. M. Yuan, Versatile code DLAYZ for investigating population kinetics and radiative properties of plasmas in non-local thermodynamic equilibrium, High Energy Density Phys. **9**, 583 (2013).

[53] B. F. Rozsnyai, Relativistic Hartree-Fock-Slater calculations for arbitrary temperature and matter density, Phys. Rev. A **5**, 1137 (1972).

[54] P. Debye and E. Hückel, The theory of electrolytes. I. Freezing point depression and related phenomena, Phys. Z. **24**, 185 (1923).

[55] Y. J. Li, C. Gao, J. L. Zeng, and J. M. Yuan, Effects of single-photon double photoionization and direct double Auger decay on K-shell ionization kinetics of Ar atoms interacting with XFEL pulses, J. Phys. B: At. Mol. Opt. Phys. **55**, 025002 (2022).

[56] C. Gao, J. L. Zeng, and J. M. Yuan, Single- and double-core-hole ion emission spectroscopy of transient neon plasmas produced by ultraintense x-ray laser pulses, J. Phys. B: At. Mol. Opt. Phys. **49**, 044001 (2016).

[57] C. Gao, Y. J. Li, J. L. Zeng, and J. M. Yuan, Ultrafast nonequilibrium ion and electron dynamics of a neon plasma produced by ultra-intensex-ray pulse, High Energy Density Phys. **23**, 217 (2017).

[58] M. Sweeney, Thermodynamic inconsistency of the modified Saha equation at high pressures, Astrophys. J. **220**, 335 (1978).

[59] C. A. Iglesias, and F. J. Rogers, Updated OPAL opacities, Astrophys. J. **464**, 943 (1996).

[60] M. J. Seaton, Y. Yan, D. Mihalas, and A. K. Pradhan, Opacities for stellar envelopes, Mon. Not. R. Astron. Soc. **266**, 805 (1994).

[61] S. B. Hansen, J. Bauche, C. Bauche-Arnoult, and M. F. Gu, Hybrid atomic models for spectroscopic plasma diagnostics, High Energy Density Phys. **3**, 109 (2007).

[62] Q. Porcherot, J. C. Pain, F. Gilleron, and T. A. Blenski, Consistent approach for mixed detailed and statistical calculation of opacities in hot plasmas, High Energy Density Phys. **7**, 234 (2011).

[63] C. Blancard, P. Cossé, and G. Faussurier, Solar mixture opacity calculations using detailed configuration and level accounting treatments, Astrophys. J. **745**, 10 (2012).

[64] J. C. Pain, and F. Gilleron, Accounting for highly excited states in detailed opacity calculations, High Energy Density Phys. **15**, 30 (2015).

[65] C. J. Fontes, C. L. Fryer, A. L. Hungerford, P. Hakel, J. Colgan, D. P. Kilcrease, and M. E. Sherrill, Relativistic opacities for astrophysical applications, High Energy Density Phys. **16**, 53 (2015).

[66] R. M. More, S. B. Hansen, and T. Nagayama, Opacity from two-photon processes, High Energy Density Phys. **24**, 44 (2017).

[67] M. Krief, Y. Kurzweil, A. Feigel, and D. Gazit, The effect of ionic correlations on radiative properties in the solar interior and terrestrial experiments, Astrophys. J. **856**, 135 (2018).

[68] J. Colgan, D. P. Kilcrease, N. H. Magee, M. E. Sherrill, J. Abdallah Jr., P. Hakel, C. J. Fontes, J. A. Guzik, and K. A. Mussack, A new generation of Los Alamos opacity tables, Astrophys. J. **817**, 116 (2016).

[69] C. A. Iglesias and S. B. Hansen, Fe XVII opacity at solar interior conditions, Astrophys. J. **835**, 284 (2017).

[70] J. E. Bailey, T. Nagayama, G. P. Loisel, G. A. Rochau, C. Blancard, J. Colgan, Ph. Cosse, G. Faussurier, C. J. Fontes, F. Gilleron et al., A higher-than-predicted measurement of iron opacity at solar interior temperatures, Nature (London) **517**, 56 (2015).

[71] T. Nagayama, J. E. Bailey, G. P. Loisel, G. S. Dunham, G. A. Rochau, C. Blancard, J. Colgan, P. Cosse, G. Faussurier et al., Systematic study of L-shell opacity at stellar interior temperatures, Phys. Rev. Lett. **122**, 235001 (2019).

[72] J. L. Zeng, C. Gao, P. F. Liu, Y. J. Li, C. S. Meng, Y. Hou, D. D. Kang, and J. M. Yuan, Electron localization enhanced photon absorption for the missing opacity in solar interior, Sci. China Phys. Mech. Astron. **65**, 233011 (2022).

[73] J. L. Zeng and J. M. Yuan, Radiative opacity of gold plasmas studied by a detailed level-accounting method, Phys. Rev. E **74**, 025401(R) (2006).

[74] J. L. Zeng and J. M. Yuan, Spectrally resolved opacities and Rosseland and Planck mean opacities of lowly ionized gold plasmas: A detailed level-accounting investigation, Phys. Rev. E **76**, 026401 (2007).

[75] Z. Jiao-Long, G. Zhao, and J. M. Yuan, Detailed radiative opacity studies of a high-temperature gold plasma, Chin. Phys. Lett. **23**, 660 (2006).

[76] J. L. Zeng, F. T. Jin, and J. M. Yuan, Radiative opacity of plasmas studied by detailed term (level) accounting approaches, Front. Phys. China **1**, 468 (2006).

[77] Z. He, J. Zhang, J. Yang, B. Yan, and Z. Hu, Time-resolved K-shell x-ray spectra of nanosecond laser-produced titanium tracer in gold plasmas, Chin. Phys. B **32**, 015202 (2023).

[78] M. S. Cho, K. Matsuo, S. Fujioka, S. J. Hahn, B. I. Cho, H. K. Chung, Opacity calculation for aluminum, iron, and gold plasmas using FLYCHK code, J. Quant. Spectrosc. Radiat. Transf. **257**, 107369 (2020).

[79] P. Troussel, B. Villette, B. Emprin, G. Oudot, V. Tassin, F. Bridou, F. Delmotte, and M. Krumrey, Absolute radiant power measurement for the Au M lines of laser-plasma using a calibrated broadband soft X-ray spectrometer with flat-spectral response, Rev. Sci. Instrum. **85**, 013503 (2014).

[80] E. M. Apfelbaum, Calculations of electrical conductivity of Ag and Au plasma, Contrib. Plasma Phys. **52**, 41 (2012).

[81] E. M. Apfelbaum, The electron transport coefficients of boron and silicon plasma, Contrib. Plasma Phys. **53**, 317 (2013).

[82] M. Oujja, J. J. Camacho, M. Sanz, M. Castillejo, and R. de Nalda, Optical diagnostics of gold plasmas produced by infrared laser ablation, J. Quant. Spectrosc. Radiat. Transf. **256**, 107308 (2020).